

Morphological and Structural Control of Electrodeposited ZnO Thin Films and Its Influence on the Photocatalytic Degradation of Methyl Orange Dye

Francisco A. Cataño¹, Humberto Gomez^{1,*}, Enrique A. Dalchiele², Ricardo E. Marotti²

¹Instituto de Química. Facultad de Ciencias, Pontificia Universidad Católica de Valparaíso, Av. Universidad 330, Curauma, Valparaíso, Chile.

²Instituto de Física & CINQUIFIMA, Facultad de Ingeniería, Herrera y Reissig 565, C.C. 30, 11000 Montevideo, Uruguay.

*E-mail: hgomez@ucv.cl

Received: 25 September 2013 / Accepted: 17 November 2013 / Published: 8 December 2013

The electrochemical synthesis, the structural, morphological and optical characterization together with the photocatalytic activity of nanostructured ZnO films prepared from zinc nitrate aqueous solutions is reported. Changes in both, the precursor concentration and the electrodeposition time allows obtaining morphologies which evolve from nanoneedles and nanorods to thin films. The analysis of texture coefficients, particle sizes and SEM images give information regarding some aspects related to the crystalline growth of the films. The photocatalytic activity was tested following the degradation of methyl orange. Results show that the surface area, the crystalline planes exposed, the morphology and the band gap of the ZnO nanostructured thin films play an important role in this activity.

Keywords: Zinc oxide, electrodeposition, heterogeneous photocatalysis, water treatment, texture coefficients.

1. INTRODUCTION

Heterogenous photocatalysis has been considered as an alternative for removing pollutants in aqueous phase due to the possibility of using solar light as energy source and atmospheric oxygen as oxidant agent [1]. It is a process by which free radicals are generated through the creation and subsequent separation of electron-hole pairs formed in a semiconductor material in the presence of light, that are capable of breaking up complex organic molecules into smaller fragments [2]. The free photogenerated holes can oxidize the organic matter adsorbed on the semiconductor surface whereas those trapped in the surface do the same with the organic remaining in solution [3]. Dissolved oxygen

can act as an electron acceptor resulting in superoxide anions formation which through a series of reactions generates hydrogen peroxide [4, 5]. An additional mechanism of photocatalytic degradation of organic pollutants takes place when organic dyes are oxidized by a photosensitization process [6]. In this case, instead of the semiconductor is the dye that is excited by visible light transferring electrons to the conduction band and creating a radical cation. The electrons injected to the conduction band can produce the oxygen reduction initiating then a reaction sequence that involves the dye degradation.

Zinc oxide is a direct wide-band-gap semiconductor with a band-gap of 3.37 eV, coupled with a large exciton binding energy of 60 meV (at room temperature). ZnO is suitable for use in a wide range of optical and electronic applications. It is also notable that ZnO is biocompatible and exhibits high mechanical, thermal, and chemical stability. Thus, a wide range of applications includes, among others, biosensors [7], optoelectronic [8], solar cells [9], water photoelectrolysis [10] and gas sensors [11]. Its potential use in photocatalysis has aroused great interest, as there have been several examples of ZnO displaying more impressive photocatalytic activity than widely studied titanium dioxide [12, 13], particularly in dyes degradation in aqueous solutions [6]. Among them, azo dyes [12, 14-16], a set of dyes widely used in the food and textile industries [17], which present potential mutagenic activity [18]. Li *et al* [6] reported a number of reasons to explain the different photocatalytic activity between ZnO and TiO₂. First, a greater efficiency of zinc oxide for the photogeneration of charge carriers *i.e.*, better light absorption as is evidenced when the absorption spectra of both oxides are compared. Second, an improved efficiency in the separation of the charge carriers, which is due to the fact that electron mobility in ZnO ($100\text{-}205 \text{ cm}^2\text{V}^{-1}\text{s}^{-1}$) is greater than in TiO₂ ($0.1\text{-}1.0 \text{ cm}^2\text{V}^{-1}\text{s}^{-1}$). Third, ZnO has better efficiency for the electron transfer from the excited molecules to the semiconductor conduction band in the case of the sensitized photocatalysis. Besides, in nanowires and nanorods structures ZnO presents high surface area for interfacial charge transfer and better light absorption by scattering [19]. In applications of waste water treatments the use of nanostructures supported on a substrate avoids the processes associated to the separation and recovery of the photocatalyst. On the other hand, electrodeposition is a useful and simple technique to form ZnO nanostructures onto conducting substrates at low temperatures and short deposition times [20-23].

Results on the synthesis, characterization and photocatalytic activity studies of nanostructured zinc oxide films obtained by electrodeposition from zinc nitrate aqueous solutions are presented in current work. It is reported that the growth of dense films or nanostructures (nanorods or nanowires arrays) can be simply controlled by tuning the zinc concentration in the electrolytic bath. The photocatalytic activity was tested following the degradation of azo dye methyl orange and results interpreted in terms of morphological, optical and structural properties of the electrodeposited nanostructured films.

2. EXPERIMENTAL

2.1. ZnO Electrodeposition

The electrodeposition of ZnO films was performed in a typical three electrode cell. The working electrodes were glass slides covered with fluor doped tin oxide thin films (FTO, 2 cm x 2 cm), the reference electrode was a Ag/AgCl_(sat) and a platinum wire has been used as counterelectrode. FTO

substrates were successively rinsed with de-ionized water and dimethyl ketone in an ultrasonic bath. Electrodeposition potential was controlled by a Gamry Serie G750 potentiostat. The electrolytic solutions were prepared with zinc nitrate (Merck P.A.) at 0.01 M, 0.03 M, 0.05 M and 0.1 M concentrations. Argon was bubbled in order to eliminate dissolved oxygen. The electrodeposition of the ZnO films has been conducted at a constant potential and with an electrolytic bath temperature of 80 °C. Total charge density exchanged (TCDE) values of 0.7 C/cm² and 1.4 C/cm² were employed for each studied zinc nitrate concentration. Additionally, a 0.10 M solution was used to deposit ZnO with a TCDE = 1 C/cm².

2.2. Structural, morphological and optical characterization

The structural characterization was carried through X-ray diffraction (XRD) measurements. Standard $\theta - 2\theta$ scans were performed on a Philips PW180 diffractometer (30 kV, 40 mA, CuK α radiation with $\lambda = 1.5406 \text{ \AA}$). The diffraction peaks from ZnO and FTO have been indexed by reference to the JCPDS powder diffraction files. SEM images were recorded from a JEOL JSM/5900 LV SEM instrument. Optical properties were studied by Transmission spectroscopy using a Shimadzu UV mini 1240 spectrophotometer.

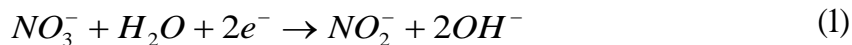
2.3. Photocatalytic activity test

The photocatalytic activity was carried out employing a 1000 W Xe/Hg lamp (Oriel 6295) as light source. In order to avoid the overheating of the methyl orange solution, the infrared radiation was eliminated through a water filter. The ZnO films deposited on FTO glass substrates were immersed in a quartz cell containing 15 mL of a 20 ppm dye solution. In order to reach the adsorption equilibrium the samples were held one hour in the dark with permanent air bubbling for also assuring dissolved oxygen saturation at the beginning of the photocatalytic degradation process. The experiments were performed for 4 hours, and samples were taken every hour. The dye concentration was measured with the absorption at $\lambda_{\max} = 465 \text{ nm}$, the respective values extracted from a previously recorded calibration curve.

3. RESULTS AND DISCUSSION

3.1. Structural characterization

ZnO nanostructured films were potentiostatically formed at a potential $E = -0.8 \text{ V}$ vs Ag/AgCl_(sat) from Zn(NO₃)₂ solutions of zinc oxide, Zn²⁺ ions react with OH⁻ ions to form Zn(OH)₂ (hydroxylation) prior to the conversion to ZnO (dehydration), according to the following well-known mechanism [24]:



Previous cyclic voltammetry results (not shown), indicate that the reduction of nitrate ions occurs at potentials more negative than -0.5 V. However, at potentials of -0.6 V and -0.7 V, the electrodeposits are of poor quality, and a potential of -0.8 V is required to obtain homogeneous films.

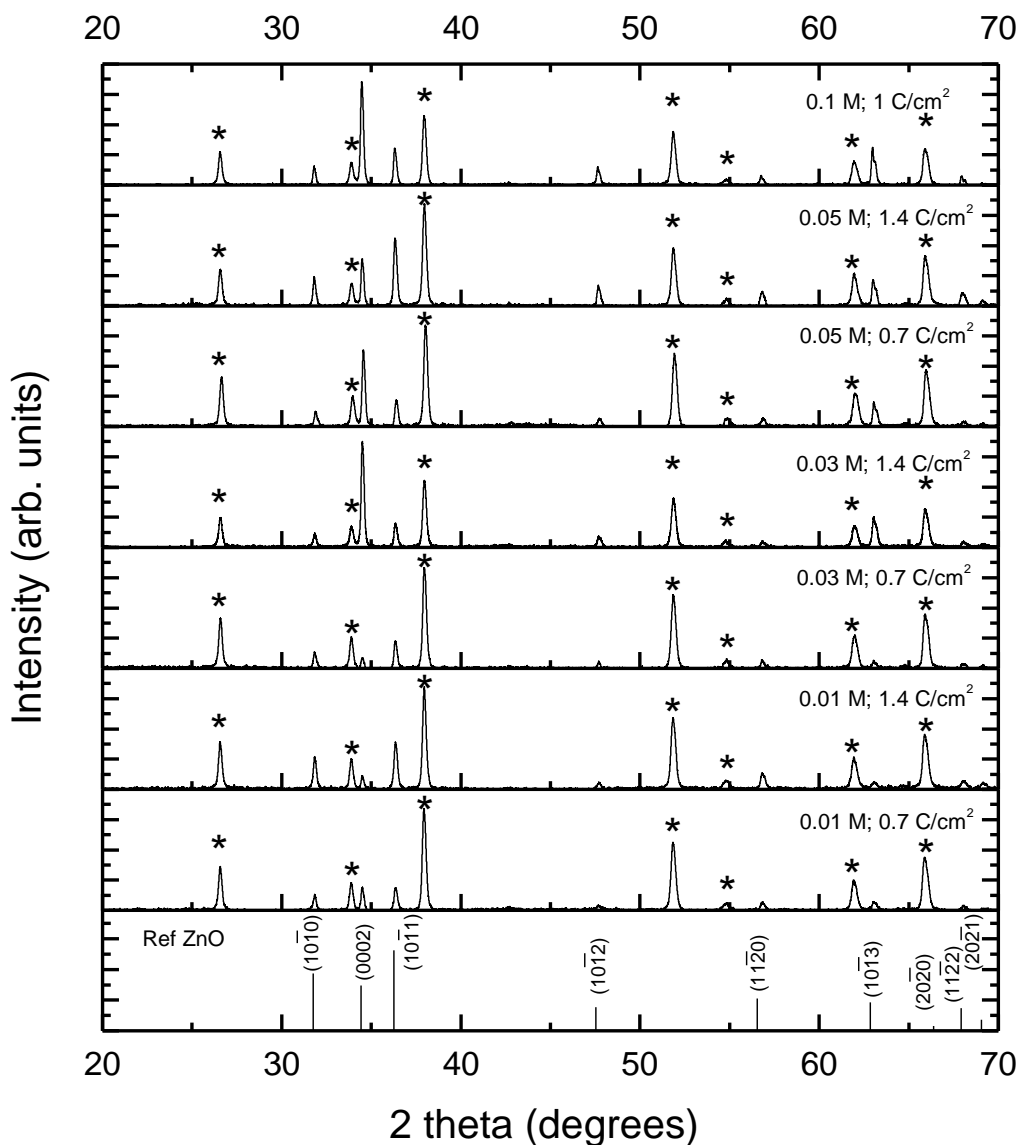


Figure 1. X-ray diffraction patterns of ZnO samples electrodeposited at $E = -0.800$ V vs. Ag/AgCl(sat) at different precursor zinc concentrations (C) and total charge density exchanged (TCDE) values, as indicated. ZnO hexagonal wurtzite JCPDS pattern is also shown for comparison in the bottom of the figure. (*) indicates the peaks originated from the SnO₂:F substrate.

In order to study the structural properties of the zinc oxide films, *i.e.*: to investigate the crystallographic phase, the overall crystalline quality, and the possible texture of those electrochemically grown thin films, X-ray diffraction experiments were carried out. The X-ray diffraction patterns (Figure 1) reveal the presence of diffraction peaks related to the hexagonal wurzite phase [25] and also those corresponding to the tetragonal SnO₂ phase [26] of FTO/glass used as a substrate. The intensity of the diffraction peaks relative to the background demonstrates a very good crystallinity of the samples. Moreover, no spurious phases were detected by XRD indicating high purity of the hexagonal ZnO phase.

To quantify the preferred crystallographic orientations of the samples and the evolution of this parameter with deposition conditions, the texture coefficient, TC, was evaluated through the following expression [27]:

$$TC(hkil) = \frac{I(hkil)/I_0(hkil)}{\left(\frac{1}{N} \left[\sum I(hkil)/I_0(hkil) \right] \right)} \quad (4)$$

where: I(hkil) is the measured peak intensity, I₀(hkil) the JCDPS standard intensity and N the total number of diffraction peaks. In general, TC is close to 1 for a powder sample randomly distributed whereas is greater than 1 when the hkil plane is preferentially oriented. The calculated TCs of ZnO thin film samples are presented in Table 1 for the three low diffraction index peaks, namely (10̄10), (0002) and (10̄11). It can be appreciated that the samples presented preferential orientation along the (0002) plane, except those obtained at 0.01 M, 1.4 C/cm² and 0.03 M; 0.7 C/cm². The high values of the (0002) TC suggest that the growth of the nanostructured films is along the c-axis normal to the substrate, confirmed by SEM observations (*vide infra*), which reveal that the nanostructured ZnO films are constituted by hexagonal prisms oriented along the largest axis. Although the dependence between the texture coefficient with the total charge density exchanged and Zn(NO₃)₂ concentration is not evident, a parallel analysis with SEM images allow for some conclusions for explaining the texture coefficient variations along the (0002) plane (*vide infra*).

Table 1. Texture coefficients for (10̄10), (0002), (10̄11) lattice planes obtained from X-ray diffraction patterns of ZnO samples electrodeposited at E = -0.800 V vs. Ag/AgCl_(sat) at different precursor zinc concentrations (C) and total charge density exchanged (TCDE) values, as indicated.

Sample C;TCDE	Texture coefficients TC(hkil)		
	(10̄10)	(0002)	(10̄11)
0.01 M; 0.7 C/cm ²	0.978	1.812	1.004
0.01 M; 1.4 C/cm ²	1.277	0.666	1.305
0.03 M; 0.7 C/cm ²	1.015	0.803	1.205
0.03 M; 1.4 C/cm ²	0.375	3.543	0.453
0.05 M; 0.7 C/cm ²	0.486	3.170	0.609
0.05 M; 1.4 C/cm ²	0.711	1.453	1.171
0.1 M; 1 C/cm ²	0.432	3.028	0.605

The mean crystallite size of the films can be estimated from the peak width at the half maximum of the diffraction peaks by using the Scherrer equation [28]:

$$D = \frac{K\lambda}{\beta \cos \theta} \quad (5)$$

where K is a constant close to 1 (K = 0.94 was used), λ_x is the X-ray wavelength whose value is 1.54 Å (CuK α), β is the full width at half maximum (FWHM) of the peak, while θ is the Bragg angle at the center of the peak.

Diffraction peaks corresponding to the (10̄10), (0002), (10̄11) lattice planes were selected to calculate those crystallite sizes. Depending on the electrodeposition conditions and the [hkl] direction considered, the calculated crystallite size values vary between 13 and 18 nm. In general, the size along the [0002] direction is greater than that calculated from the other planes (except for the 0,1M; 1C/cm² sample). This suggests that the length of the crystallites measured along this [0002] direction is greater than the characteristic dimensions in the other directions, resulting in an elongated form of the crystal [29], meaning then that the ZnO crystals are both, columnar in shape and anisotropic [30]. It can be mentioned that previous studies also reported that the most stable ZnO crystal structure is a hexagonal prism elongated along the c-axis, as the maximal growth velocity is fixed in this direction [30, 31].

3.2. Morphological characterization

SEM images (Figure 2) of the films show that the morphology changes with the precursor concentration and the total charge density exchanged. A change of ten times in zinc ions concentration changes the morphology from nanoneedles and nanorods to dense films. Increases in charge density leads to increases both the height and the diameter of nanoneedles and nanorods, the increases being greater in height than in diameter (height was estimated from 45° tilted SEM images). At a concentration of 0.05 M a two times increases in charge density entails an increase of nanorods diameter to form a dense film. Another interesting feature is that at low concentrations (0.01 M) appear morphologies that exhibit characteristics of both, nanoneedles and nanorods. This means that the dimension of the hexagonal cross section undergoes a slight decrease from the bottom to the top of the structure. The opposite occurs at 0.03 M and 0.05 M concentrations where the hexagonal cross section remains unchanged. Table 2 summarizes the morphological characteristics for the nanoneedles and nanorods samples, the aspect ratio (length/diameter) and the $S_{real}/S_{geometric}$ values, the latter corresponding to the ratio between the actual exposed area of zinc oxide and the geometric area. It can be calculated from:

$$\frac{S_{real}}{S_{geométrico}} \approx N\pi DL \quad (6)$$

where N is the nanostructures density, D and L their average diameters and heights, respectively.

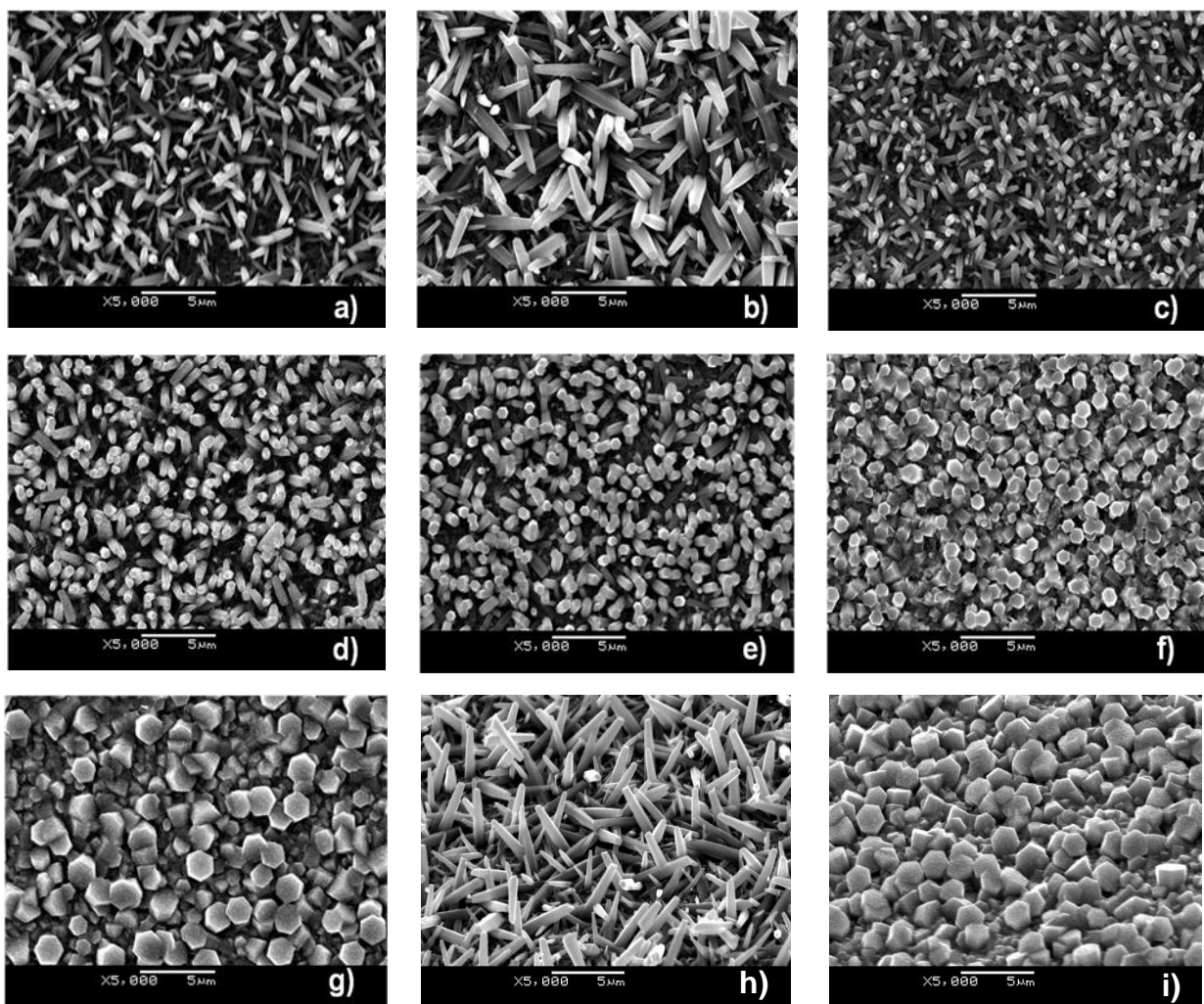


Figure 2. SEM images for ZnO samples grown at $E = -0.800$ V vs. Ag/AgCl(sat) at different precursor zinc concentrations (C) and total charge density exchanged (TCDE) values: a.) 0.01 M; 0.7 C/cm² b.) 0.01 M; 1.4 C/cm² c.) 0.03 M; 0.7 C/cm² d.) 0.03 M; 1.4 C/cm² e.) 0.05 M; 0.7 C/cm² f.) 0.05 M; 1.4 C/cm² g.) 0.1 M; 1 C/cm² h) and i) 45° tilted Images for 0.01 M; 1.4 C/cm² and 0.1 M; 1 C/cm² respectively.

Table 2. Morphological characteristics of nanostructured ZnO samples electrodeposited at $E = -0.800$ V vs. Ag/AgCl_(sat) at different precursor zinc concentrations (C) and total charge density exchanged (TCDE) values, as indicated.

Sample C;TCDE	Diameter		Average height (μm)	Density (10 ⁸ cm ⁻²)	$S_{\text{real}}/S_{\text{geometrico}}$	Aspect ratio
	Average (μm)	Standard deviation (μm)				
0.01 M; 0.7 C/cm ²	0.35	0.15	1.49	2.00	3.25	4.25
0.01 M; 1.4 C/cm ²	0.45	0.24	2.00	1.22	3.43	4.44
0.03 M; 0.7 C/cm ²	0.36	0.10	1.16	1.98	2.59	3.22
0.03 M; 1.4 C/cm ²	0.44	0.12	1.86	1.32	3.40	4.22
0.05 M; 0.7 C/cm ²	0.49	0.14	1.11	1.62	2.78	2.26

With increasing of both, the precursor concentration and the total charge density exchanged, the diameter of the nanoneedles and nanorods also increases. Besides, at 0.01 M the standard deviation in diameter values is greater, indicating a wider diameters distribution in the samples. For the 0.05 M; 1.4 C/cm² and 0.1 M; 1 C/cm² conditions is difficult to get an estimation of the S_{real}/S_{geometric} ratio from SEM images. In this case the values were obtained from the analysis of AFM images (not shown) giving 1.43 and 1.40 for 0.05 M; 1.4 C/cm² and 0.1 M; 1 C/cm² respectively. Therefore these samples were those that presented a lower surface area.

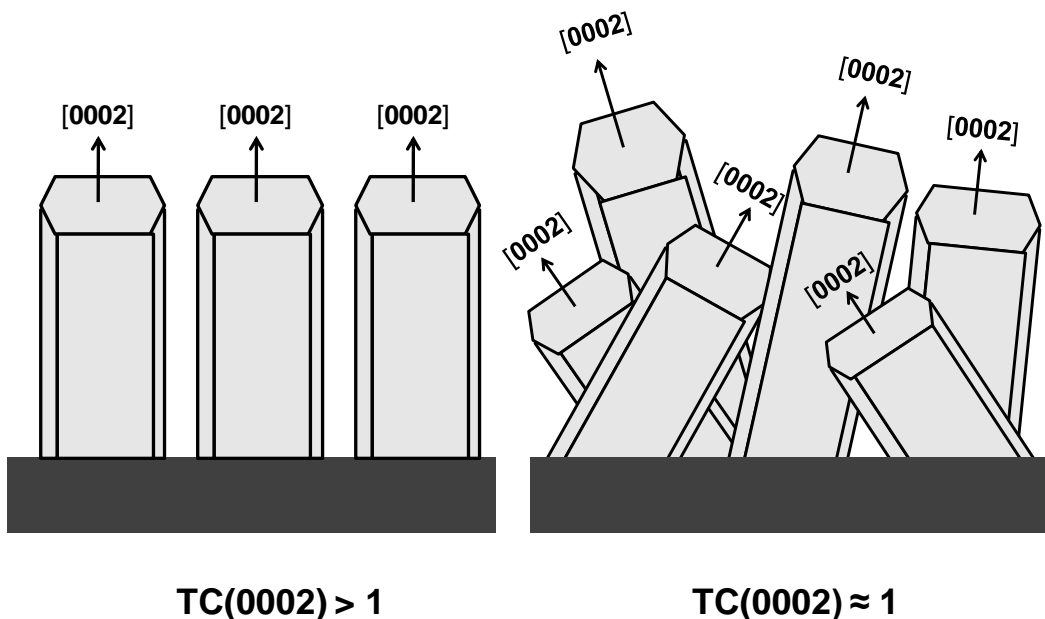


Figure 3. Scheme for the crystalline growth of electrodeposited ZnO films.

TC values along the [0002] direction and SEM images shows an increase when nanoneedles and nanorods structures grow vertically to the substrate. Sample 0.03 M, 1.4 C/cm² exhibits the highest (0002) TC value, whereas the 0.01 M, 1.4 C/cm² sample, that grows inclined respect to the substrate, has the lower value. The dependence of (0002) TC on morphology together with the elongated form of the nanostructures along the [0002] direction suggests that the crystalline growth of ZnO is as shown in Figure 3, except for the 0.10 M, 1 C/cm² sample which does not exhibits an elongated form along the same direction. It has been reported that electrodeposited ZnO nanowires grow along the [0002] direction, coinciding with the nanowires axis [32].

3.3. Optical characterization

The UV-VIS transmittance spectra of the samples are shown in Figure 4. They present a monotonically decay with an interference pattern in the visible region, followed by an absorption band between 370 and 390 nm corresponding to electron transitions from the valence to the conduction band.

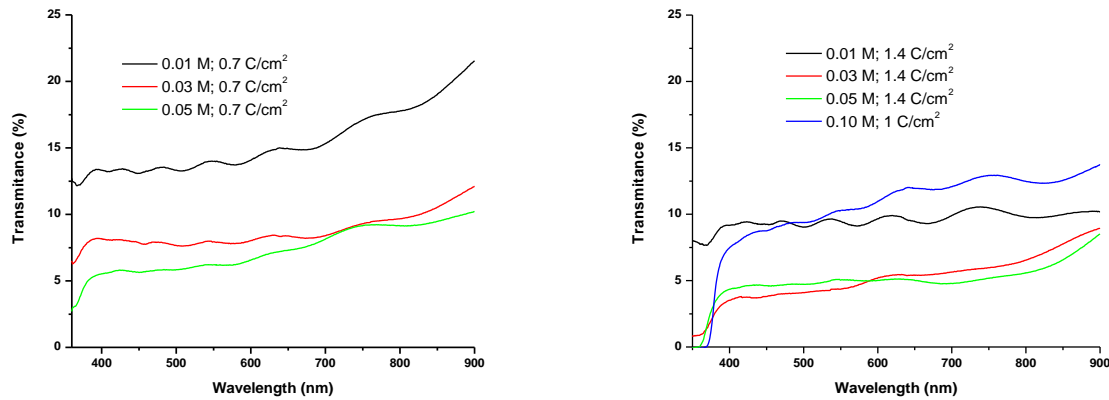


Figure 4. UV-vis transmittance spectra for ZnO samples grown at $E = -0.800$ V vs. Ag/AgCl(sat) at different precursor zinc concentrations (C) and total charge density exchanged (TCDE) values as indicated.

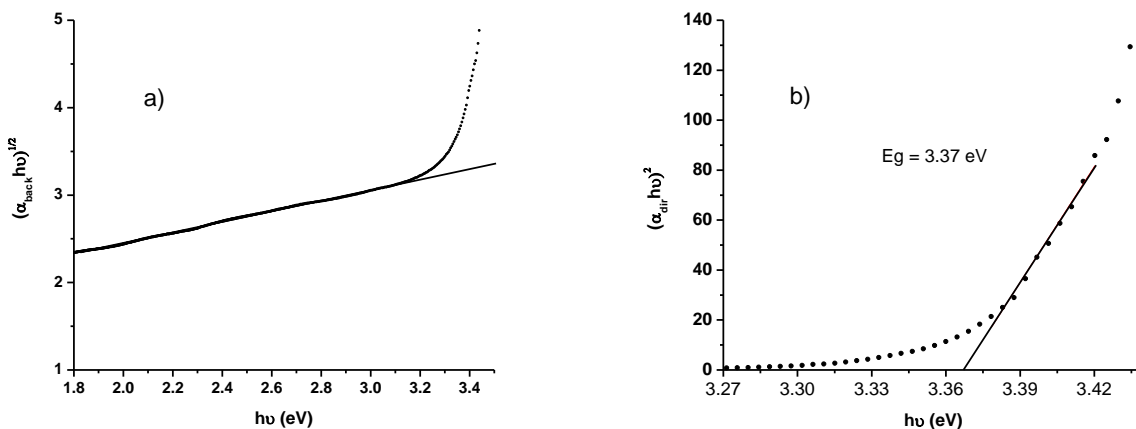


Figure 5. Examples of plots for deriving the bandgap energy values (sample grown at $E = -0.800$ V vs Ag/AgCl(sat) at a $C=0.05$ M and TCDE = 1.4 C/cm 2) a) α_{back} estimation; b) E_g value.

For semiconductors presenting direct transitions the bandgap energy can be obtained by a linear fitting of $(\alpha h\nu)^2$ vs $h\nu$ plot. The methodology considered reflection, dispersion and sub bandgap absorption processes which were modeled as an indirect absorption coefficient [33]. The expressions used were:

$$\alpha \approx -\ln(T) \quad (7)$$

$$\alpha = \alpha_{back} + \alpha_{dir} \quad (8)$$

where T: transmittance; α_{dir} : direct absorption coefficient; α_{back} : indirect absorption coefficient. α_{back} is deduced from the linear regression of the $(\alpha h\nu)^{1/2}$ vs $h\nu$ plot and then subtracted from α to get

α_{dir} . Figure 5 illustrates the application of the method for obtaining the bandgap energy values which results are summarized in Table 3.

Table 3. Bandgap energy values (in eV) for nanostructured ZnO samples electrodeposited at $E = -0.800$ V vs. Ag/AgCl_(sat) at different precursor zinc concentrations (C) and total charge density exchanged (TCDE) values, as indicated.

C and TCDE	0.7 C/cm ²	1.4 C/cm ²
0.01 M	3.26	3.24
0.03 M	3.31	3.30
0.05 M	3.30	3.37
0.1 M; 1 C/cm ²	3.30	

3.4. Photocatalytic test

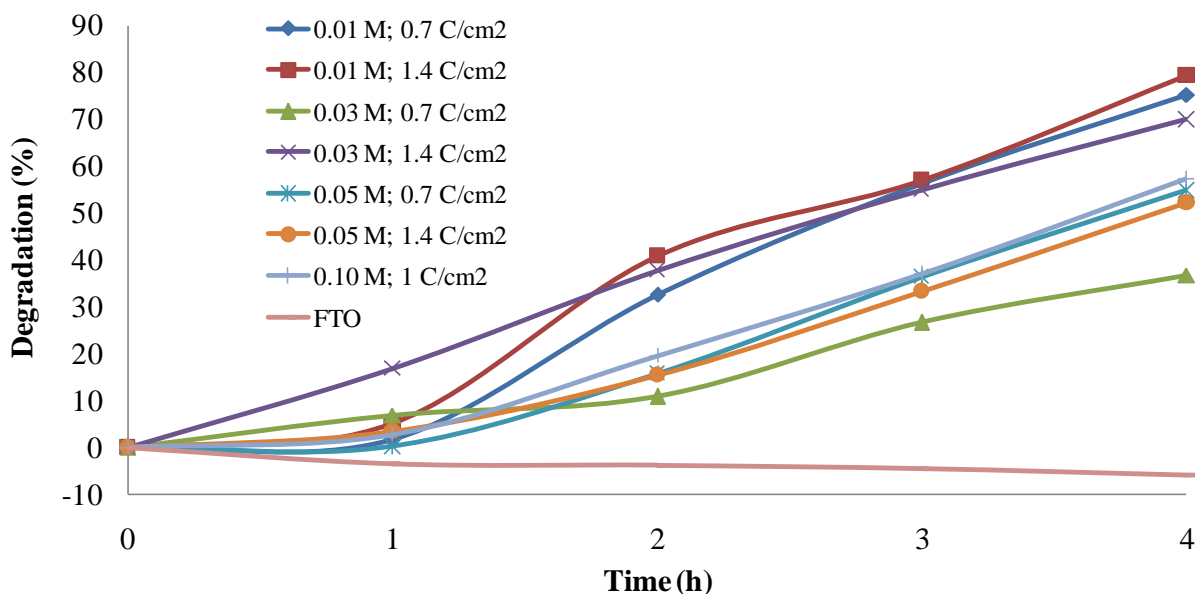


Figure 6. Percentage of methyl orange degradation as a function of illumination time for different ZnO nanostructures (indicated by the zinc concentration and TCDE values employed during their synthesis).

The photocatalytic activity of the ZnO nanostructures has been evaluated in terms of the degradation percentage of methyl orange dye as a function of illumination time. Figure 6 presents this photocatalytic activity for different ZnO nanostructures (identified by the zinc concentration and TCDE values employed during their synthesis). When a bare FTO/glass substrate was immersed in the dye solution and after illumination a negligible decolorization was observed, while a significant decolorization was observed when FTO with deposited zinc oxide nanostructures was illuminated. The observed decolorization can be attributed to the degradation of methyl orange by heterogeneous photocatalysis of nanostructured zinc oxide. It has been established that the photocatalysed degradation

of organic matter in solution by a semiconductor is initiated by photoexcitation of the semiconductor, followed by the formation of an electron-hole pair. The high oxidative potential of the hole in the valence band lead to the oxidation of organic matter to reactive intermediates [3]. Oxidation can also occur by photosensitization of ZnO or possibly by the reaction with hydrogen peroxide and radical intermediates formed by the reduction of oxygen [19].

Li et al [6] demonstrate the photocatalytic degradation of methyl orange using microscale ZnO and visible light ($\lambda > 420$ nm). As the photocatalyst does not absorb light in that range of wavelenghts, the only possible mechanism of degradation is by a photosensitized oxidation. In our case the range of wavelenghts used was between ~240 nm and ~950 nm, so we can expect both, a photosensitized oxidation when visible light is absorbed by the dye, and a direct oxidation by holes in valence band when the semiconductor absorb UV light. Another aspect involved in the mechanism of degradation is the production of hydrogen peroxide. Harbor and Hair [5] studied the formation of hydrogen peroxide when ZnO powders dispersion in an oxygenated aqueous medium are illuminated. This process begins with the reduction of oxygen by electrons in conduction the band to form $O_2^{\cdot-}$ and HO_2^{\cdot} adsorbed on the semiconductor surface.

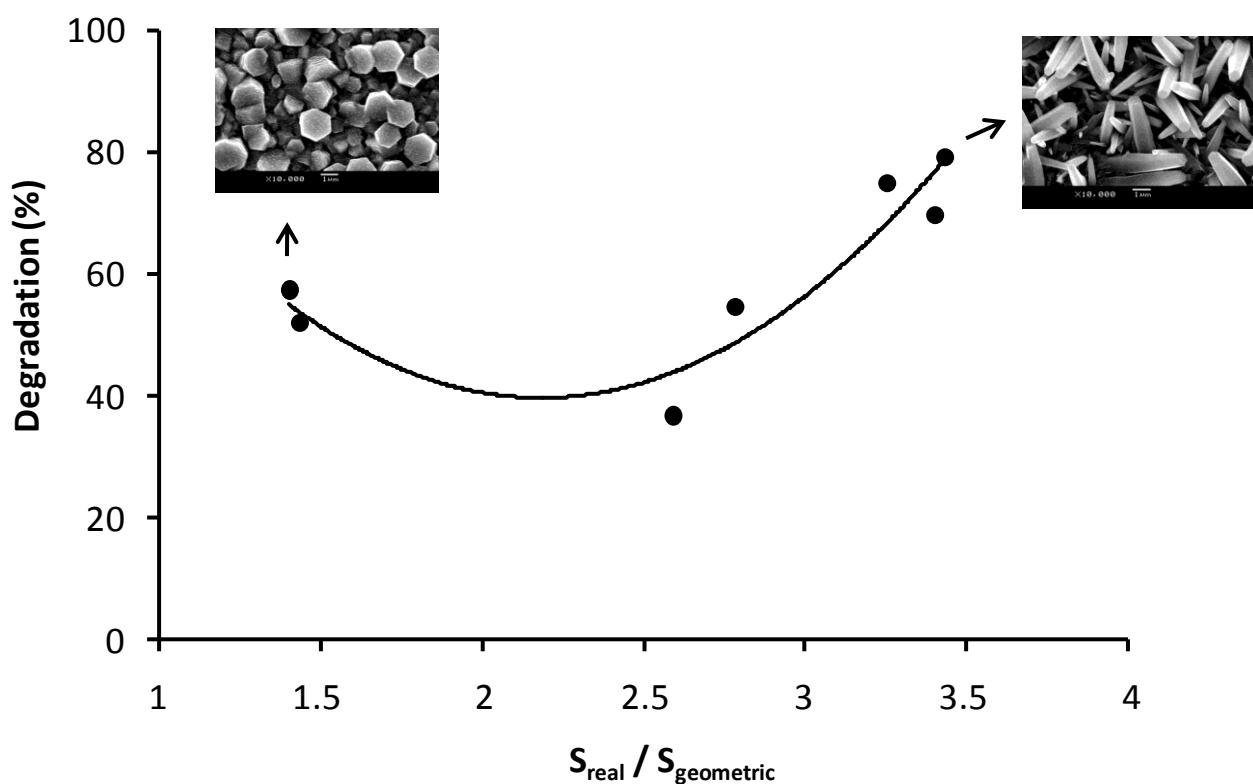


Figure 7. Dependence of the percentage of degradation at 4 hours of illumination with surface area and morphology.

Then hydrogen peroxide is formed by the reduction and protonation of HO_2^{\cdot} . The photolysis of hydrogen peroxide (eq. 9) is possible because the quantum yield of this reaction at 254 nm is 0.5 [34].



The hydroxyl radical is a highly oxidant agent and can produce the degradation of methyl orange. Initially, the reaction between hydroxyl radical and methyl orange produce the hydroxylation of the aromatic rings and demethylation of the amine group [35]. Also, the radical hydroxyl attack the C-N bond far from the electron attracting group ($-SO_3^-$) [36]. This process lead to the aromatic ring-opening and continuos oxidation, finally a serie of carboxylic acids are produced before the formation of CO_2 [37].

In particular, the photocatalytic activity has been further evaluated as the degradation percentage value after 4 hours of illumination. The photocatalytic activity evaluated in this way for the different nanostructured ZnO samples (named in the basis of their synthesis conditions, i.e. precursor zinc concentrations and total charge density exchanged values), exhibits the following sequence: 0.01 M; $1.4\text{ C}/\text{cm}^2 > 0.01\text{ M}$; $0.7\text{ C}/\text{cm}^2 > 0.03\text{ M}$; $1.4\text{ C}/\text{cm}^2 > 0.1\text{ M}$; $1\text{ C}/\text{cm}^2 > 0.05\text{ M}$; $0.7\text{ C}/\text{cm}^2 > 0.05\text{ M}$; $1.4\text{ C}/\text{cm}^2 > 0.03\text{ M}$; $0.7\text{ C}/\text{cm}^2$. As it is well established, the photocatalytic activity is in general directly dependent on the surface area, a greater area provide more active sites for contacting the pollutant with the photocatalyst. According to Table 2, the samples with greater surface area were those that presented also a greater degradation percentage. Figure 7 shows the variation of the latter with the $S_{\text{real}}/S_{\text{geometric}}$ ratio. For values over 2.5 it is clearly seen that the increase in the surface area entails an increase in the photocatalytic activity. These points are associated to nanorod and nanoneedle morphologies. However, $S_{\text{real}}/S_{\text{geométrico}}$ ratios of 1.4 and 1.43 deviate from the trend because the photocatalytic activity is higher than expected, they correspond to samples that presented more compact and dense morphologies (0.1 M; $1\text{ C}/\text{cm}^2$ and 0.05 M; $1.4\text{ C}/\text{cm}^2$). One possible explanation of this behavior is related to the fact that the photocatalytic activity depends on the crystallographic planes exposed to the pollutant molecules.

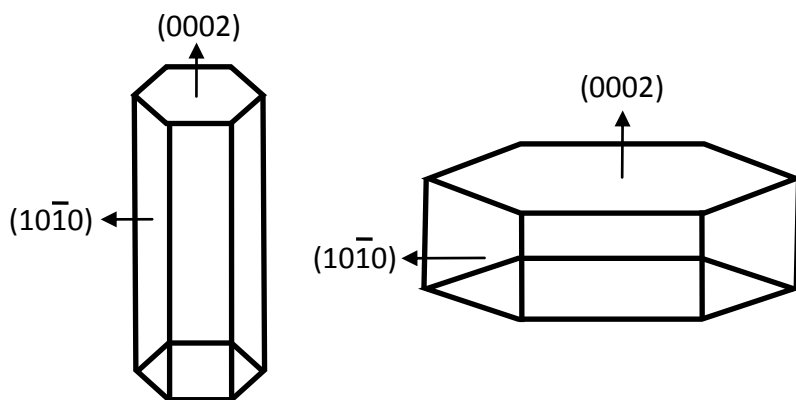


Figure 8. Scheme illustrating the exposed planes for two different morphologies.

Assuming that hexagonal surfaces correspond to the (0002) polar planes (as illustrated in Figures 3 and 8), the active photocatalytic surface can be mainly associated to the (0002) polar planes finished in zinc ((0001)-Zn) or oxygen ((0001)-O). It has been reported that (0002) polar planes have

grater photocatalytic activity than the perpendicular non-polar sidewalls {1010} planes [38]. As the (0001)-Zn plane finished in zinc presents positive charge and oxygens vacancies it can absorb molecular oxygen and hydroxyl ions which entails an increase in the production of hydrogen peroxide and hydroxyl radicals [39]. Another aspect that may explain the different photocatalytic activity between non-polar and polar planes is that they present different coordinations of zinc and oxygen atoms at the surface. Such differences in the surface chemistry may alter the interactions between methyl orange molecules with the photocatalyst surface and the interfacial charge transfer processes both directly influencing the catalytic photoactivity.

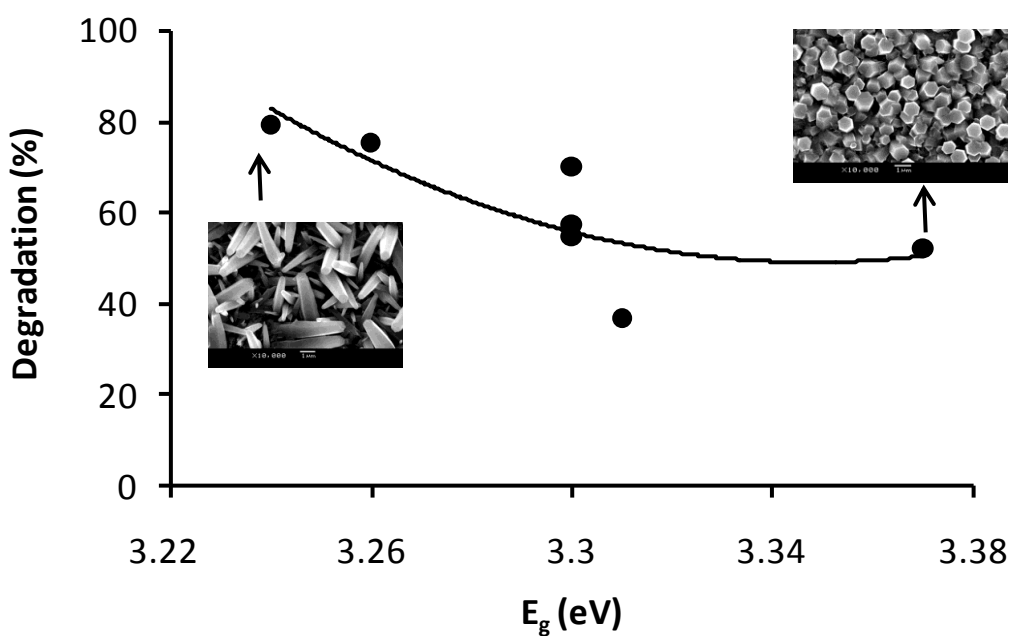


Figure 9. Dependence of the percentage of degradation at 4 hours of illumination with bandgap energy and morphology.

Another aspect that has direct influence in heterogenous catalysis is the semiconductor energy bandgap. Low bandgap values entail a greater spectral response, therefore a better generation of electron-hole pairs. For the electrodeposited ZnO nanostructures the E_g values varied between 3.24 and 3.37 eV, which in terms of wavelengths correspond to a variation of 15 nm (368 nm – 383 nm). Although is a small wavelength interval it can be considered enough for evaluating the influence in the photocatalysis since in this range there is an emssion band of the lamp ($\lambda_{\text{max}} = 365$ nm). Figure 9 shows the dependence of the degradation percentage with band-gap energy. As is observed in the figure, lower band-gaps are associated to greater photocatalytic activity. This is a relevant information because in current study we have achieved a methodology to tailoring the energy band gap and surface area through the control of precursor concentration and the charge density during ZnO electrodeposition. Once again dense morphologies with (0002) faces exposed presents a better photocatalytic activity than expected.

4. CONCLUSIONS

ZnO nanostructured thin films were obtained by electrodeposition at constant potential from zinc nitrate solutions. Through changes in precursor concentration and charge density it was possible to tailor the morphology and structural characteristics of the films. The morphologies varied from nanoneedles and nanorods to dense films. XRD analysis showed that these films had wurtzite hexagonal structure. The joint analysis of the crystallite sizes along different directions, the texture coefficients and SEM images suggest that for nanoneedles and nanorods there is a preferential growth along the [0002] direction. The determination of the band-gap energy was performed taking into account an indirect like absorption dependence with photon energy for obtaining the zero of absorption associated to the band to band transitions. All the electrodeposited films were tested for the photocatalytic degradation of methyl orange dye. As expected, films with greater surface area and lower energy band gap exhibited the better performance. These results were also interpreted by assuming that the (0002) polar planes present greater photocatalytic activity than the non polar perpendicular planes.

ACKNOWLEDGMENTS.

This work has been supported by FONDECYT (Fondo de Desarrollo Científico y Tecnológico, Chile) through grant N° 1110619. F.A.C. acknowledges the support received from the Vicerrectoría de Investigación y Estudios Avanzados, Pontificia Universidad Católica de Valparaíso (Project 037.445/2012) and also to CONICYT (Comisión Nacional de Investigación Científica y Tecnológica de Chile) for the doctoral scholarship awarded. E.A.D. and R.M. thank to CSIC (Comisión Sectorial de Investigación Científica) of the Universidad de la República, in Montevideo, Uruguay, PEDECIBA – Física, ANII (Agencia Nacional de Investigación e Innovación), Uruguay.

References

1. S. Malato, P. Fernández-Ibañez, M.I. Maldonado, J. Blanco, W. Gerjank, *Catal. Today*, 147 (2009) 1.
2. J.M Herrmann, *Catal. Today*, 53 (1999) 115.
3. D. Monllor-Satoca, R. Gómez, M. González-Hidalgo, P. Salvador, *Catal. Today*, 129 (2007) 247.
4. P. Salvador, *J. Phys. Chem. C*, 111 (2007) 17038.
5. J.R. Harbour, M.L. Hair, *J. Phys. Chem.*, 83 (1979) 652.
6. Y. Li, W. Xie, X. Hu, G. Shen, X. Zhou, Y. Xiang, X. Zhao, P. Fang, *Langmuir*, 26 (2010) 591.
7. S.K. Arya, S. Saha, J.E. Ramirez-Vick, V. Gupta , S. Bhansali, S.P. Singh. *Anal. Chim. Acta*, 737 (2011) 1.
8. A.B. Djurisic, A.M.C. Ng, X.Y. Chen, *Prog. Quantum. Electron.*, 34 (2010) 191.
9. V.M. Guerin, J. Rathousky, Th. Pauporté, *Sol. Energy. Mat. Sol. Cells*, 102 (2012) 8.
10. N.K. Hassan, M.R. Hashim, N.K. Allam, *Chem. Phys. Lett.*, 549 (2012) 62.
11. J.J. Hassan, M.A. Mahdi, C.W. Chin, H. Abu-Hassan, Z. Hassan. *Sensor. Actuat. B.* 176 (2013) 360.
12. S.K. Kansal, M. Singh, D. Sud, *J. Hazard. Mater.*, 141 (2007) 581.
13. M.C. Yeber, J. Rodríguez, J. Freer, J. Baeza, N. Durán, H.S. Mansilla, *Chemosphere*, 39 (1999) 1679.
14. A. Akyol, H.C. Yatmaz, M. Bayramoglu, *Appl Catal B*, 54 (2004) 19-24.

15. M. Kositzi, I. Poulios, K. Samara, E. Tsatsaroni, E. Darakas, *J. Hazard. Mater.*, 146 (2007) 680.
16. S. Sakthivel, B. Neppolian, M.V. Shankar, B. Arabindoo, M. Palanichamy, V. Murugesan, *Sol. Energ. Mat. Sol. Cell.*, 77 (2003) 65.
17. N. Guettai, A. Amat, *Desalination*, 185 (2005) 427.
18. R.O. Alves de Lima, A.P. Bazo, D.M. Fávero, C.M. Rech, D. Oliviera, G. Umbuzeiro, *Mutat. Res.*, 626 (2007) 53.
19. Y. Liu, J. Han, W. Qiu, W. Gao, *Appl. Surf. Sci.*, 263 (2012) 389.
20. D. Pradhan, K.T. Leung, *Langmuir*, 24 (2008) 9707.
21. G. Guerguerian, F. Elhordoy, C.J. Pereyra, R.E. Marotti, F. Martin, D. Leitnen, J.R. Ramos-Barrado, E.A. Dalchiele, *Nanotechnology*, 22 (2011) 505401.
22. H. Gómez, G. Riveros, D. Ramirez, R. Henriquez, R. Schrebler, R.E. Marotti, E.A. Dalchiele, *J. Solid. State. Electrochem.*, 16 (2012) 197.
23. A. Tello, H. Gómez, E. Muñoz, G. Riveros, C.J. Pereyra, E.A. Dalchiele, R.E. Marotti, *J. Electrochem. Soc.*, 159 (2012) D750.
24. T. Yoshida, D. Komatsu, N. Shimokawa, H. Minoura, *Thin Solid Films*, 451-452 (2004) 166.
25. JCPDS, 5-0664, ZnO, 1992.
26. JCPDS, 41-1445, SnO₂ 1999.
27. J.A. Rivera, C.M. Bautista, C. Mendoza, E. Rubio, O. Zelaya, O. Tzili, *Int. J. Electrochem. Sci.*, 6 (2011) 4059.
28. B.D. Cullity, Elements of X-ray Diffraction, second ed., Addison-Wesley, Reading, MA, 1978.
29. R.E. Marotti, P. Giorgi, G. Machado, E.A. Dalchiele, *Sol. Energy. Mat. Sol. Cells*, 90 (2006) 2356.
30. C.T. Hsieh, S.Y. Yang, J.L. Gu, Y.R. Jiang, *Solid State Ionics*, 209-210 (2012) 43.
31. X.F. Yuan, J.P. Tu, H.M. Wu, B. Zhang, X.H. Huang, X.B. Zhao, *J. Electrochem. Soc.*, 153 (2006) A1719.
32. [32] J. Elias, R. Tena-Zaera, C. Léy-Clément. *J. Electroanal. Chem.*, 621 (2008) 171.
33. C.D. Bojorge, V.R. Kent, E. Teliz, H.R. Cánepa, R. Henríquez, H. Gómez, R.E. Marotti, E.A. Dalchiele, *Phys. Status. Solid. A*, 208 (2011) 1662.
34. J.C. Crittenden, S. Hu, D.W. Hand, S.A. Green, *Wat. Res.*, 33 (1999) 2315.
35. Y. He, F. Grieser, M. Ashokkumar, *Ultrason. Sonochem.*, 18 (2011) 974.
36. Y-P. Chen, S-Y. Liu, H-Q. Yu, H. Yin, Q-R. Li, *Chemosphere*, 72 (2008) 532.
37. E. Isarain-Chávez, C. de la Rosa, C.A. Martínez-Huitl, J.M. Peralta-Hernández, *Int. J. Electrochem. Sci.*, 8 (2013) 3084.
38. N. Talebian, M.R. Nilforoushan, N. Maleki, *Thin Solid Films*, 527 (2013) 50.
39. L. Zhang, L. Yin, C. Wang, N. Lun, Y. Qi, *ACS. Appl. Mater. Interfaces*, 2 (2010) 1769.